

# Antiferromagnet-topological insulator heterostructure for polarization-controllable terahertz generation

Received: 7 March 2025

Accepted: 13 May 2025

Published online: 01 July 2025

 Check for updatesYu Cheng<sup>1,2,8</sup>, Faran Zhou<sup>1,2,8</sup>, Jing Teng<sup>1,2</sup>  , Peiyan Li<sup>3,4</sup>, Litong Jiang<sup>1,2</sup>, Piming Gong<sup>1,2</sup>, Yongqing Li<sup>1,2</sup>, Xiaojun Wu<sup>3,4,5</sup>, Franz X. Kärtner<sup>6</sup> & Jimin Zhao<sup>1,2,7</sup>  

Antiferromagnets (AFMs) are more advantageous in realizing ultrafast spin-based processes, but remain challenging to manipulate. The lack of proper knobs in AFM-based ultrafast devices greatly hampers their applications. Here, we innovate an antiferromagnet/topological insulator (AFM/TI) heterostructure MnSe/(Bi,Sb)<sub>2</sub>Te<sub>3</sub> to realize laser-induced transient magnetic moment, and further demonstrate optically controllable circularly polarized ultrafast terahertz (THz) pulse generation, under zero external magnetic field. Intriguingly, we find two mechanisms underlying the ultrafast THz pulse generation: direct magnetic dipole radiation and spin-charge conversion resulted electric dipole radiation. Our findings provide a suitable platform for efficient and polarization-controllable ultrafast THz devices via optical means.

Antiferromagnetic materials exhibit strong exchange couplings that result in ultrafast spin dynamics in terahertz regime<sup>1–3</sup>. The overall zero magnetic moment and stability under an external magnetic field make antiferromagnets promising candidates for high-density, high-speed, and low-dissipation spintronic applications<sup>4–6</sup>. The AFM/TI heterostructures have been found exhibiting novel static chiral spin transport<sup>7</sup> and high spin-charge conversion efficiency<sup>8–12</sup>. Moreover, the magnetic proximity effect can induce emergent phenomena such as exchange bias<sup>13–16</sup>, topological transitions<sup>17</sup>, and geometric Hall effect<sup>18,19</sup>. However, such an excellent capability of an AFM/TI structure in tuning spin degree of freedom<sup>20,21</sup> is previously mainly with static devices. It has not been explored for ultrafast performances.

Conventionally, spin current generation and spin-flip transition in devices are controlled by external magnetic or electric fields<sup>11,12,22,23</sup>. As a comparison, ultrafast optical excitation stands out owing to its ultrafast speed, high energy efficiency, and strong control performance without auxiliary fields. In recent years, ultrafast THz emission

spectroscopy has emerged as a powerful technique to study the spin and charge dynamics, which is by detecting the THz pulse emission upon optical excitation. Successful THz pulse emission advancements have been reported along this line<sup>24–33</sup>, mostly belonging to only a handful of structures. It has been thought that an AFM/TI structure is potentially promising to realize both fast spin dynamics and efficient spin-charge conversion, sometimes without external field. However, AFM/TI structure has never been realized for THz emission, due to the lack of proper AFM and TI materials to form a lattice-matched heterostructure.

Here, we demonstrate an ideal material system for an AFM/TI heterostructure, MnSe/(Bi,Sb)<sub>2</sub>Te<sub>3</sub>, for THz generation, which offers a unique platform for tuning the frequency, intensity, and polarization of THz emission by ultrafast manipulation of the antiferromagnetic order alongside a topological surface state. By near-infrared ultrafast excitation, we generate light-induced transient magnetization and ultrafast spin current in a MnSe/(Bi,Sb)<sub>2</sub>Te<sub>3</sub> nanofilm on Al<sub>2</sub>O<sub>3</sub>

<sup>1</sup>Beijing National Laboratory for Condensed Matter Physics and Institute of Physics, Chinese Academy of Sciences, Beijing 100190, China. <sup>2</sup>School of Physical Sciences, University of Chinese Academy of Sciences, Beijing 100049, China. <sup>3</sup>Hangzhou International Innovation Institute, Beihang University, Hangzhou 311115, China. <sup>4</sup>School of Electronic and Information Engineering, Beihang University, Beijing 100191, China. <sup>5</sup>Zhangjiang Laboratory, 100 Haik Road, Shanghai 201210, China. <sup>6</sup>Center for Free-Electron Laser Science, Deutsches Elektronen-Synchrotron, Notkestraße 85, Hamburg 22607, Germany. <sup>7</sup>Songshan Lake Materials Laboratory, Dongguan, Guangdong 523808, China. <sup>8</sup>These authors contributed equally: Yu Cheng, Faran Zhou. ✉ e-mail: [jteng@iphy.ac.cn](mailto:jteng@iphy.ac.cn); [jmzhao@iphy.ac.cn](mailto:jmzhao@iphy.ac.cn)

substrate, which leads to THz emission. Both magnetic dipole (MD) radiation and spin-charge conversion (SCC) induced electric dipole radiation are found as the mechanism, which enables effective polarization control of the emitted THz pulses. The AFM/TI interface plays a crucial role in the efficient SCC process. Our findings highlight a new class of heterostructures for designing high-speed, low-energy dissipation, and polarization-controllable THz spintronic devices.

## Results

### Field-free THz emission from a MnSe/(Bi,Sb)<sub>2</sub>Te<sub>3</sub> heterostructure

The schematic experimental setup is shown in Fig. 1a. Under near-infrared femtosecond laser pulse excitation, a MnSe/(Bi,Sb)<sub>2</sub>Te<sub>3</sub> (MnSe/BST) heterostructure on Al<sub>2</sub>O<sub>3</sub> substrate radiates ultrafast THz pulses without an external magnetic field at room temperature. The crystallographic and spin structures of the MnSe are illustrated in Fig. 1b. MnSe is in the type-II (G-type) AFM structure with the spins aligned along [001] direction<sup>1,34</sup>, forming an AFM order along [111] direction, which is also chosen as the z-axis. Figure 1c presents the radiated THz waveforms from the MnSe/BST heterostructure, as well as those from two control-experiment samples (MnSe and BST) under identical conditions. The measured electric field strength of THz radiation from MnSe/BST is 22.3 V/m, with the THz conversion efficiency  $\eta = 2.03 \times 10^{-8}$  at 12 nm sample thickness (Supplementary Note 10). The corresponding frequency-domain spectra obtained by Fourier transform are plotted in Fig. 1d. The effective spectral range is 0.15–3 THz. The THz radiation spectrum from MnSe/BST/substrate is broadened. In the control experiment, the spectrum from MnSe/substrate is 0.15–1.8 THz and that from BST/substrate is negligible. Thus, the broadening can only come from the synthetic combination of MnSe and BST, the AFM/TI interface<sup>24</sup>. The MnSe film is an AFM insulator with a bandgap of 2.0 eV (larger than the 1.55 eV excitation photon energy), having a low SCC efficiency<sup>1,35</sup> (its Hall angle is nearly negligible). Thus, we expect the electric-dipole-induced THz emission (generated by photocurrent, optical rectification or SCC)<sup>24,25,35,36</sup> from MnSe/substrate to be very weak. However, its experimentally observed value is of the same order of that of MnSe/BST/substrate. This indicates that, other than the regular SCC-induced electric dipole emission in magnetic-nonmagnetic heterostructure, there exists other emission mechanism(s). In addition, the negligible THz radiation from the BST film excludes the linear photo-galvanic effect (PGE) as the emission mechanism in the heterostructure<sup>37,38</sup>.

### Dependence of THz emission on the excitation laser polarization

Keeping the sample fixed, we rotate the excitation laser pulse polarization to control the THz emission pulses (Fig. 2). Figure 2a shows the time domain THz waveforms depending on the excitation linear laser polarization angle  $\theta$ . Correspondingly, we do the FFT of the data in Fig. 2a to obtain the frequency-domain spectra at various  $\theta$  (Fig. 2b). In both figures, the amplitude and waveform have a prominent dependence on  $\theta$ , exhibiting an overall two-fold rotational symmetry, which is different from that in the FM/HM case dominated by the SCC mechanism<sup>30,36</sup>. Moreover, the two-fold rotational symmetry is composed of two different sinusoidal components, marked by different colors and separated by two lines in Fig. 2a. In Fig. 2b, the corresponding FFT spectrum also exhibits identical symmetries, with the four lobes separated by identical lines at identical angles. For example, the major peak at 0.6 THz is a single peak from 157° to 262° and a double peak from 82° to 157°. We interpret that this unusual polarization-dependent behavior is driven by more than one underlying emission mechanism in our sample. To see this more clearly, we plot the THz peak values at 2.6 ps and 3.3 ps (Fig. 2a) in Fig. 2c as functions of  $\theta$ . Each curve exhibits a period of 180°, thus together manifesting two independent two-fold rotational symmetries. The two periodic curves exhibit polarity reversals at 82°

and 157° within a 180° period, explaining why there are four lobes in Fig. 2a, b. This indicates that there are two THz radiation mechanisms in MnSe/BST heterostructure.

It has been shown that circular PGE in TI films<sup>38</sup>, inverse Faraday effect<sup>39</sup>, and laser-induced transient magnetization<sup>40,41</sup> can all be responsible for the laser-polarization-controlled THz emission. To analyze the mechanism, we carry out circular-polarization excitation experiments. In Fig. 2d, the THz waveforms under left- and right-circular polarization excitations are plotted, which are perfectly in phase with nearly identical amplitude. Their sum is lower than that under linear polarization excitation. These facts exclude the inverse Faraday effect<sup>39</sup> and the circular PGE<sup>42</sup> as the underlying mechanism, because in both cases the waveforms under left- and right-circular excitations are of opposite sign (with equal amplitude), and that under linear excitation is inactive<sup>39</sup> or relatively weak<sup>42</sup>. Hence, the remaining candidate can be laser-induced transient magnetization. We also measure the pump-fluence dependence of the generated THz *E*-field at  $\theta = 30^\circ$  and  $t = 2.6$  ps (Fig. 2e), whereby the THz signal is the strongest. The emission amplitude linearly depends on the pump fluence, indicating no laser heating is observed, up to 0.03  $\mu\text{J cm}^{-2}$ . This linear dependence is in line with the mechanism of light-induced transient magnetization<sup>25,40</sup>.

### Experimental evidence of the two THz emission mechanisms

For spintronic devices based on magnetic-nonmagnetic heterostructures, many works reported the mechanism for THz radiation as SCC; only for a few samples the THz emission mechanism is assigned to MD. Both the SCC and MD mechanisms are generated from the magnetization  $\mathbf{M}(t)$  of the sample. However, to date, there is very rare report of co-existed two mechanisms. Here, we show our crucial experimental evidence for the SCC mechanism, light-induced transient magnetization  $\mathbf{M}(t)$ , and MD mechanism. The total THz radiation is determined by both the SCC and MD mechanisms (see Supplementary Note 3 for the radiation process).

**Experimental evidence of the SCC mechanism.** To elucidate the underlying mechanism, we first investigate the THz emission under different geometries by flipping the sample while fixing the pump polarization at 0° (along the *y*-axis). Flipping the sample around the *x*-axis, the polarity of the THz waveform is not affected (Fig. 3a, up-down flip), although the waveform experiences a 2.9 ps time delay due to the refractive index of the Al<sub>2</sub>O<sub>3</sub> substrate. In contrast, flipping the sample around the *y*-axis (Fig. 3a, left-right flip), the THz signal polarity is reversed. These observations together form the experimental evidence that SCC is one of the THz emission mechanisms in the sample, which is attributed to the inverse Rashba-Edelstein effect at the TI surface<sup>24,26,37</sup>. In the SCC mechanism,  $\mathbf{E}_{\text{THz}} \propto \mathbf{J}_c \propto \alpha_{\text{SH}} (\mathbf{J}_s \times \boldsymbol{\sigma}(t))$ , where  $\mathbf{J}_c$  is the converted charge current,  $\alpha_{\text{SH}}$  is the spin Hall angle,  $\mathbf{J}_s$  is the spin current, and  $\boldsymbol{\sigma}(t) = \mathbf{M}/|\mathbf{M}|$  is the spin polarization. Flipping the sample along the *x*-axis will reverse  $\boldsymbol{\sigma}(t)$ , but flipping along the *y*-axis will not. Both will reverse  $\mathbf{J}_s$ , which injects from the MnSe layer to the BST layer<sup>24,26</sup>. Hence the polarity variation under flips (Fig. 3a) can be fully explained by the SCC mechanism. Note that our AFM/TI sample has zero net magnetization. Considering that MnSe/substrate can also produce THz radiation under excitation, we interpret that a light-induced magnetization component along the *y*-axis ( $\Delta M_y$ ) is realized in MnSe layer, which leads to the spin polarization  $\boldsymbol{\sigma}(t)$  and spin current  $\mathbf{J}_s$ .

**Experimental evidence of light-induced magnetization  $\mathbf{M}(t)$ .** To verify the light-induced magnetization, we investigate the THz emission at different sample azimuth  $\alpha$  by rotating the sample around the *z*-axis. In Fig. 3b, the THz signal peak values are plotted as a function of the sample azimuth  $\alpha$  for both MnSe/substrate (upper panel) and MnSe/BST/substrate (lower panel). Both data show a three-fold rotational symmetry with a period of 120°, which is consistent with the symmetry of the MnSe (111) lattice plane. Similar

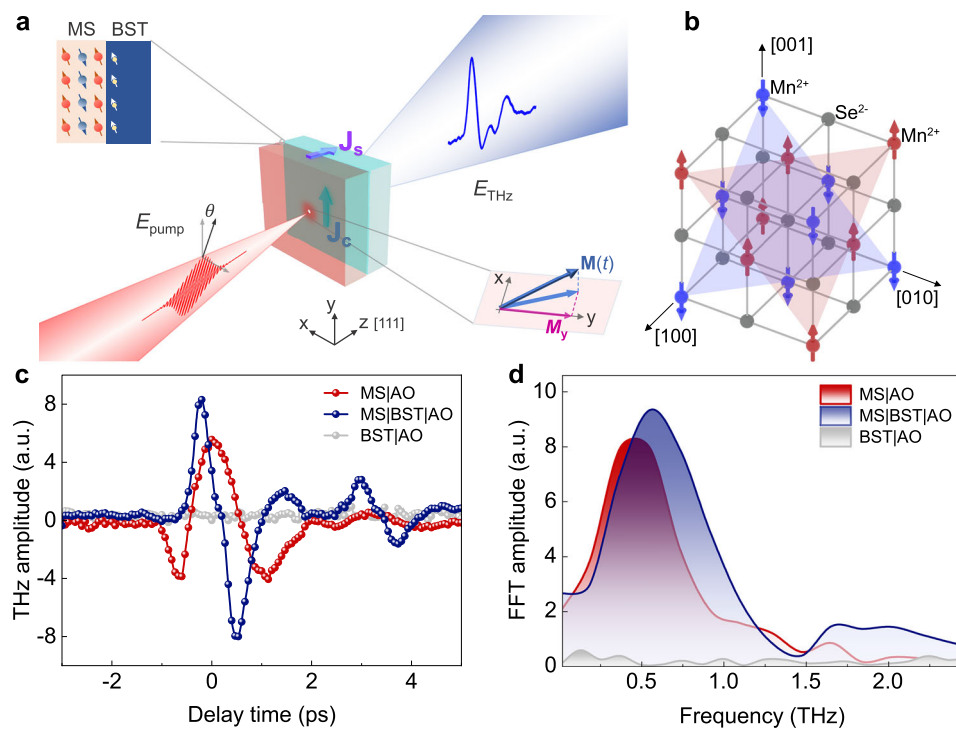


**Fig. 1 | Experimental setup and THz emission spectrum.** **a** Schematic of the THz emission spectroscopy setup. The coordinates ( $xyz$ ) are adapted to the laboratory frame. **b** Crystallographic and magnetic structure of MnSe. The spins of  $\text{Mn}^{2+}$  forms an AFM order along  $[111]$  direction. **c** Waveforms of the THz emission from MnSe

(8 nm)/ $\text{Al}_2\text{O}_3$  (0.5 mm) (abbreviated as MS/AO), MnSe (8 nm)/BST (4 nm)/ $\text{Al}_2\text{O}_3$  (0.5 mm), and BST (4 nm)/ $\text{Al}_2\text{O}_3$  (0.5 mm), labelled in red, blue, and gray colors, respectively. **d** Corresponding frequency domain (fast Fourier transform) spectra of the THz waveforms in **c**. a.u., arbitrary units.

three-fold periodicity of THz emission had been reported in NiO film<sup>25,40</sup>, which is also a type-II AFM with identical point group to MnSe. In such type of materials, transient magnetization  $\mathbf{M}(t)$  is generated by ultrafast optical excitation through a Raman-type difference frequency generation process. Because the electric field of THz emission generated by either MD or SCC mechanisms has a linear dependence on  $\mathbf{M}(t)$ , it will also exhibit the three-fold periodicity as  $\mathbf{M}(t)$ , expressed as  $E_{\text{THz}} = [A \cos(3\alpha + \phi) + B \cos(\alpha + \phi')] + C$  (see Supplementary Information Note 6 and 7), where  $A$  and  $B$  are coefficients determined by the second-order nonlinear tensor components,  $\phi$  and  $\phi'$  are phase offsets,  $C$  is a constant. The experimental data in Fig. 3b can be well-fitted by the above function, which demonstrates the existence of light-induced transient  $\mathbf{M}(t)$ .

The Néel temperature of bulk MnSe is reported to be 173 K<sup>1</sup>. However, it had been shown that the antiferromagnetic phase transition of thin film MnSe occurs over a very wide temperature range, up to near room temperature<sup>43</sup>. We measure the temperature dependence of THz emission (Fig. 3c), whose intensity monotonically decrease with increasing temperature in a linear way. This indicates there is no magnetic phase transition from 85 K to room temperature, which is consistent with the known fact that phase transition stiffness will be reduced in thinner samples<sup>44</sup>. That the THz emission intensity reduces with increasing temperature supports the existence of laser-induced transient  $\mathbf{M}(t)$ . Moreover, we apply external magnetic field (up to 230 mT) to the simply find that the external field has no effect on the polarity or amplitude of the THz emission in both MnSe/substrate and MnSe/BST/substrate. This demonstrates the external magnetic field is not strong enough to affect the spin structure in MnSe layer, which manifests the favorable robustness of AFM spintronic devices against external magnetic field.

**Experimental evidence of the MD mechanism.** From  $\mathbf{M}(t)$ , there can be SCC driven THz emission, and there can also be MD induced

radiation that is generated directly from  $\mathbf{M}(t)$ . The latter is usually weak. Because we have observed in Fig. 3a that SCC cannot fully account for the different THz intensity after flips, and we have excluded many other mechanisms by the results in Fig. 2, we contemplate that the other mechanism is the MD-induced emission, which can be described by  $E_{\text{THz}} \propto \partial^2 / \partial t^2 (\mathbf{e} \times \mathbf{M}(t))$ , where  $\mathbf{e}$  is the unit vector of radiation direction<sup>45</sup>. Such an assignment can be corroborated by the result in the upper panel of Fig. 3b. Because MnSe is insulating (thus SCC is negligible), we attribute the THz emission in MnSe/substrate to the MD mechanism.

To quantitatively investigate the two mechanisms, we first measure the THz waveforms of MnSe/substrate for various pump polarization  $\theta$ . The relation between the peak value of the THz waveform and  $\theta$  is shown in Fig. 3d upper panel. The THz intensity only slightly changes with  $\theta$  (deviation <8.5%), indicating that MD radiation in MnSe is nearly  $\theta$ -independence (see Supplementary Note 11). Then, the pump polarization-dependence measurement is performed on both the front and (left-right flipped) back side of the MnSe/BST/substrate sample. The peak values of the THz signals are summarized in Fig. 3d lower panel, with the red dots adapted from Fig. 2a. The THz intensity variation is 38 times larger than that on MnSe/substrate, confirming that the THz radiation in MnSe/BST/substrate has a large contribution from the SCC mechanism. The data from both samples exhibit a cosine behavior with a period of  $180^\circ$ , thus can be well-fitted by  $S_{\text{THz}} = A_1 \cos(2\theta + \varphi) + A_2$  (solid curves in Fig. 3d lower panel). The coexistence of polarization-dependent and polarization-independent terms manifests the SCC (dependent) and MD (independent) mechanisms for the radiation. We obtain the average values  $A_1 = 13.92$  and  $A_2 = 4.28$  for the two curves. There is a phase difference  $\Delta\varphi = 85.12^\circ$ , which we attribute to the reversal of  $\mathbf{J}_s$  due to the sample flip, giving a negative sign to the coefficient  $A_1$  (i.e., the approximately  $90^\circ$  phase difference for a  $180^\circ$  period behavior). Therefore, the total radiation THz signal is quantitatively described by  $S_{\text{TOTAL}} = A_{\text{SCC}} \cos(2\theta + \varphi) + A_{\text{MD}}$ . The intensity of the two components is marked by the purple and green arrows.

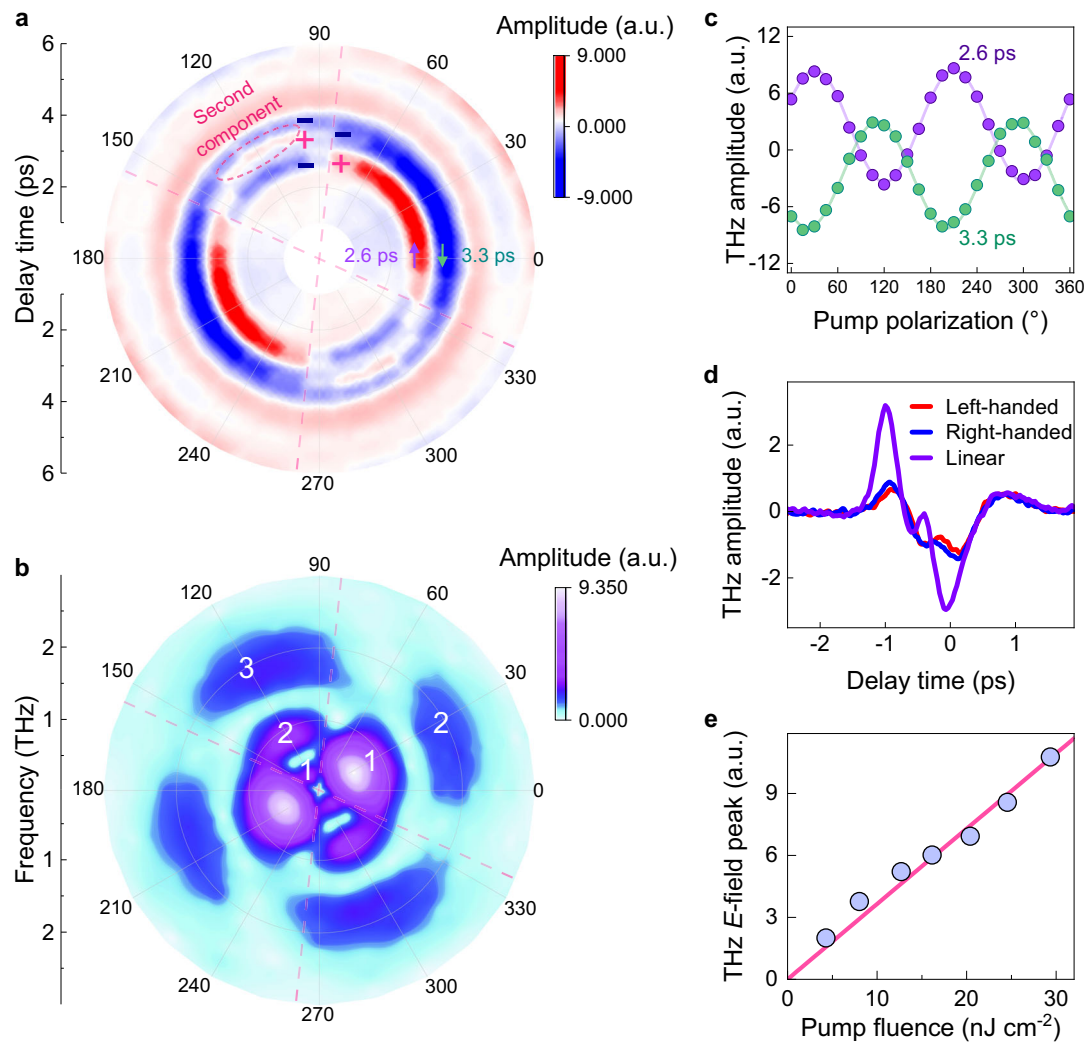


**Fig. 2 | Strong dependence of THz emission on laser polarization.** THz emission waveforms **a** for various laser polarization directions  $\theta$  and corresponding FFT spectra **b**.  $\theta = 0^\circ$  corresponds to the  $y$ -axis. “+” and “-” signs: peaks and dips of the time-domain THz waves, respectively. Numbers 1-3: frequency domain peaks. **c** The amplitude of the THz electric-field signal as a function of  $\theta$ . Green and purple markers represent the data at 2.6 ps and 3.3 ps cut in **a**, respectively. **d** Waveforms

of the THz emission under different laser polarization states. Red, blue and purple solid lines represent THz emission signals under left-handed, right-handed and linear laser polarization excitation, respectively. **e** The peak value of THz electric field as a function of the pump fluence. The solid red line is a linear fit of the data with intercept at zero.

### Controlling the polarization states of the ultrafast THz radiation

To explore the potential application of AFM/TI heterostructures in THz emission, we measure the polarization state of the radiated THz wave under different conditions using two wire-grid polarizers right in front of the detector. The first polarizer is nearest to the detector and set parallel to the  $y$ -axis. The second polarizer in front of the first polarizer is set to be either  $+45^\circ$  or  $-45^\circ$  relative to the  $y$ -axis. In this setup, the  $E_x$  and  $E_y$  components of the THz  $E$ -field are expressed as:

$$E_x = 1/\sqrt{2}(E_{+45^\circ} - E_{-45^\circ})$$

$$E_y = 1/\sqrt{2}(E_{+45^\circ} + E_{-45^\circ})$$

Figure 4b–d demonstrates the temporal evolution of the emitted THz  $E$ -field at pump polarizations of  $0^\circ$ ,  $30^\circ$ , and  $120^\circ$  in the left-right flipped sample, respectively. Significantly, the pump polarization can prominently control the polarization state of the emitted THz waves. At  $\theta = 0^\circ$ , the THz  $E$ -field is in linear polarization. At  $\theta = 30^\circ$ , the radiation polarization exhibits a trajectory that is a sequential combination of a

linear and elliptical polarization. At  $\theta = 120^\circ$ , the THz emission exhibits a left-handed circular polarization. Figure 4e–g presents the analysis on amplitude ratio and phase difference of the  $E_x$  and  $E_y$  components. In Fig. 4g, in the 1.0–3.1 THz region, the amplitude ratio is 1 and the phase difference is  $90^\circ$ , which is a perfect working zone for generating a circularly polarized ultrafast THz light pulse emission. To date, circular or elliptical spintronic THz emission has rarely been realized, although it has great application potentials in full control of THz light pulses. Our experiment demonstrates one of the best close-to-perfect circular polarization THz emission results. Excluding other mechanisms such as CPGE and Faraday effect that can produce elliptical THz emission in the MnSe/BST/substrate heterostructure, we demonstrate a route of generating circular THz waves based on AFM/TI system. It provides unprecedented circular THz emission, which can be easily controlled by tuning the pump polarization. Our AFM/TI design ensures both the amplitude ratio and phase difference between the two THz components are well controlled. This two-mechanism route, together with the AFM/TI route, achieves a performance beyond conventional spintronic THz devices. Our findings provide a technical guidance for THz polarization control in the future AFM/TI-based heterostructures.

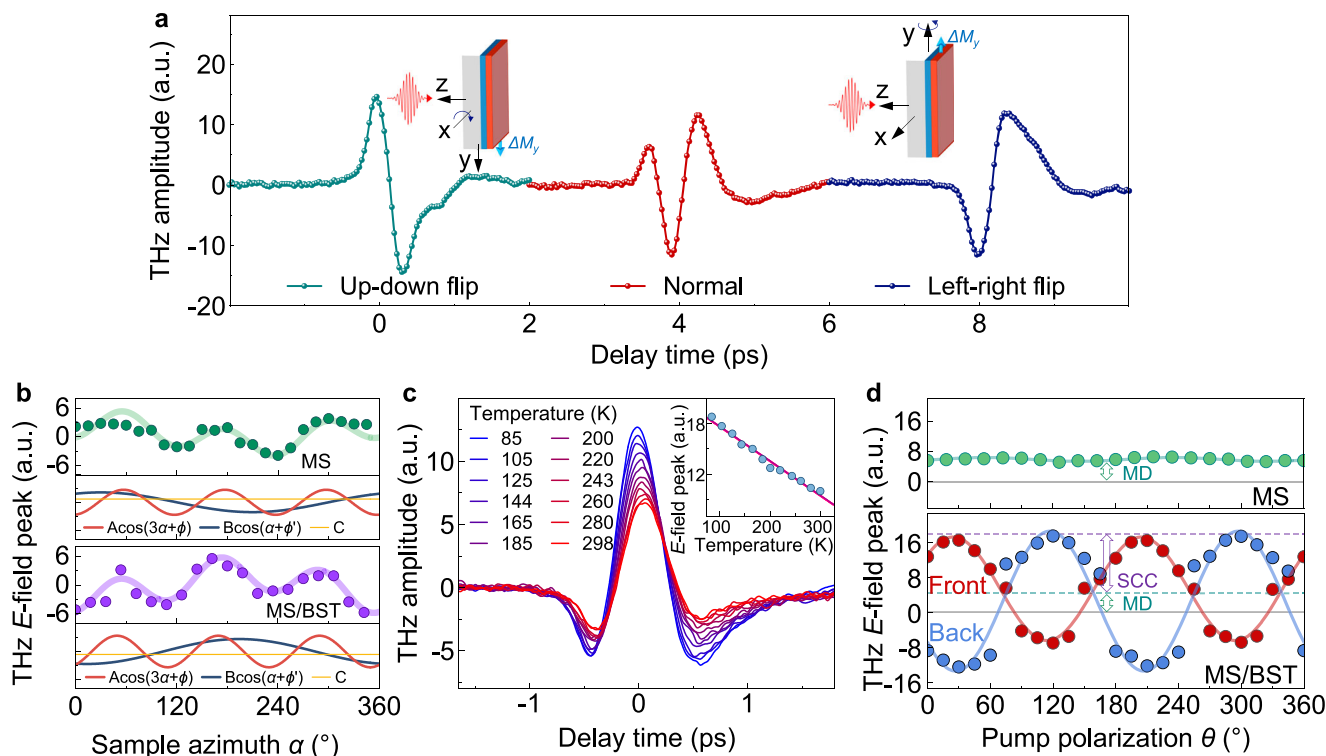


**Fig. 3 | Identification and extraction of two components of the THz emission.** **a** Sensitivity of the THz emission to  $180^\circ$  rotation of the sample along the  $x$ - and  $y$ -axis. All measurements are performed at  $\theta = 0^\circ$  without external field. **b** Dependence of THz emission amplitude on the sample azimuth  $\alpha$  for MnSe/substrate (upper panel) and MnSe/BST/substrate (lower panel). The fit (solid curves) to the experimental data (green and purple circles) is based on Eq. S8 in SI Note 7. **c** The waveforms of THz emission at different sample temperatures. The

inset is the extracted peak-to-peak value of the radiated THz signals as a function of the sample temperature, exhibiting a linear relationship. **d** THz emission amplitude for both MS substrate (upper panel) and MS/BST/substrate (lower panel) depending on  $\theta$ . The red and blue data points correspond to the front-(normal) and back-(left-right flip) excitation experimental geometry, and solid curves are the fits described in the main text. The green and purple arrows represent the intensity of THz emission contributed by MD and SCC process separately.

In our sample, two independent mechanisms combine to determine the THz emission, as shown in Fig. 4a. Upon femtosecond optical excitation, the transient  $\mathbf{M}(t)$  is first generated in the AFM layer, which is accompanied with MD radiation. At the same time, the impulsive  $\mathbf{M}(t)$  generates a spin current injecting from the AFM to TI layer. The spin current  $\mathbf{J}_s$  is converted into a transverse charge current  $\mathbf{J}_c$ , which radiates THz pulses via the electric dipole radiation. Due to such a sequence of events, there is a fixed phase difference between the MD and SCC emissions. Consequently, the elliptically polarized THz radiation can be attributed to the superposition of two non-parallel THz fields generated by the two mechanisms, which has not been reported before. Note that the emissions from the MD and SCC channels can be separately controlled, by tuning the pump beam polarization and/or sample azimuth. The SCC and MD together determine the output THz radiation in a syngenetic way, endowing the AFM/TI type heterostructure relatively higher controllability in the polarization state over previously established spintronic emitters.

In summary, we report the room temperature ultrafast optical generation of THz emission from a novel MnSe/BST/substrate heterostructure, without external field. Light-induced transient magnetization leads to two principal THz radiation mechanisms. One is the MD mechanism in the AFM layer and the other is the SCC mechanism in the AFM/TI interface. Consequently, both the amplitude and the polarization of the THz  $E$ -field are highly tunable. Our discovery lay the foundation for AFM/TI heterostructure as a new class of spintronic THz devices, capable of generating elliptically polarized THz emission, accomplishing the last piece of jigsaw puzzle of magnetic-nonmagnetic heterostructure-based THz spintronic devices.

## Methods

### Sample preparation and characterization

The MnSe/(Bi<sub>1-x</sub>Sb<sub>x</sub>)<sub>2</sub>Te<sub>3</sub> heterostructures are grown on 0.3 mm thick heat-treated Al<sub>2</sub>O<sub>3</sub> (111) substrates in a molecule beam epitaxy system with a base pressure of  $3 \times 10^{-10}$  mbar. The Sb/Bi composition ratio is calibrated with quartz crystal microbalance and adjusted to make the Fermi level close to the charge neutral point at zero gate-voltage, which is  $x = 0.5$  throughout this work. The (Bi,Sb)<sub>2</sub>Te<sub>3</sub> layer is first grown at 270 °C, followed by the growth of the MnSe layer at 300 °C. All the MnSe/(Bi<sub>1-x</sub>Sb<sub>x</sub>)<sub>2</sub>Te<sub>3</sub> heterostructure samples investigated in this work are composed of a 3 nm thick MnSe film and a 8 nm thick (Bi,Sb)<sub>2</sub>Te<sub>3</sub> film. The growth process is monitored in situ with a reflection high-energy electron diffractometer.

### THz emission measurements

A THz time-domain emission spectroscopy system in transmission geometry is utilized to investigate the THz emission process. The pump laser comes from a Ti:sapphire oscillator (Tsunami 3941-M1BB, Spectra Physics) with 800 nm central wavelength, 100-fs pulse width, and 80 MHz repetition rate. The output of the oscillator is split into two branches: one is used for optical pumping (about 0.1  $\mu\text{J cm}^{-2}$ ), the other is used for the THz electric-field detection (0.012  $\mu\text{J cm}^{-2}$ ). A half waveplate is mounted before the sample to adjust the polarization direction of the excitation laser. The THz pulse is emitted along the  $z$ -axis, and collected and focused onto the low-temperature grown GaAs photoconductive antenna using a pair of parabolic mirrors. The entire experimental setup is placed in a plastic box purged with dry nitrogen to minimize the effects of water vapor absorption.

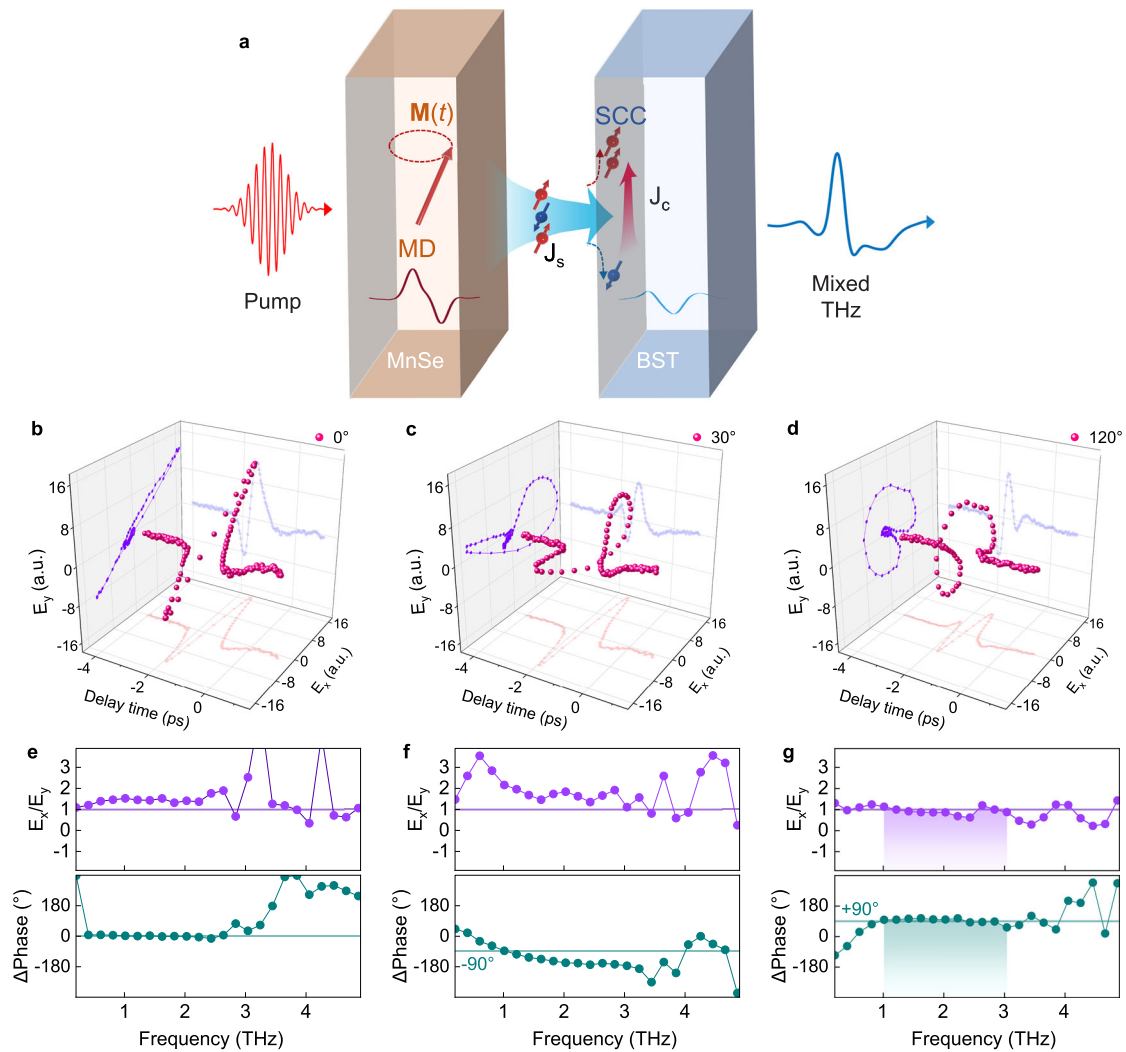


**Fig. 4 | Temporal evolution of the THz radiation under various pump polarization.** **a** Schematic diagram of the two-mechanisms THz emission process. **b–d** Electric-field trajectories of the THz emission when the pump polarization is at  $0^\circ$ ,  $30^\circ$  and  $120^\circ$ , respectively. The THz emission is modulated by the pump

polarization  $\theta$  with a period of  $180^\circ$ . **e–g**, Amplitude ratio (upper panels) and phase difference (lower panels) of the  $E_x$  and  $E_y$  components shown in **b–d**. Shaded area: working area (1.0–3.1 THz) for generating circular polarization THz radiation.

## Data availability

The data of the figures in the main text are provided in the Supplementary Information/Source Data file. Source data are provided with this paper. The data that support other findings of this study are available from the corresponding author on request. Source data are provided with this paper.

## References

- Jungwirth, T., Marti, X., Wadley, P. & Wunderlich, J. Antiferromagnetic spintronics. *Nat. Nanotechnol.* **11**, 231–241 (2016).
- Lebrun, R. et al. Tunable long-distance spin transport in a crystalline antiferromagnetic iron oxide. *Nature* **561**, 222–225 (2018).
- Baltz, V. et al. Antiferromagnetic spintronics. *Rev. Mod. Phys.* **90**, 015005 (2018).
- Zhang, S. et al. Photoinduced terahertz radiation and negative conductivity dynamics in Heusler alloy  $\text{Co}_2\text{MnSn}$  film. *Opt. Lett.* **42**, 3080–3083 (2017).
- Cheng, R., Xiao, J., Niu, Q. & Brataas, A. Spin pumping and spin-transfer torques in antiferromagnets. *Phys. Rev. Lett.* **113**, 057601 (2014).
- Safin, A. et al. Electrically tunable detector of THz-frequency signals based on an antiferromagnet. *Appl. Phys. Lett.* **117**, 222411 (2020).
- Tokura, Y., Yasuda, K. & Tsukazaki, A. Magnetic topological insulators. *Nat. Rev. Phys.* **1**, 126–143 (2019).
- Fan, Y. et al. Magnetization switching through giant spin-orbit torque in a magnetically doped topological insulator heterostructure. *Nat. Mater.* **13**, 699–704 (2014).
- Ghosh, S. & Manchon, A. Nonequilibrium spin density and spin-orbit torque in a three-dimensional topological insulator/antiferromagnet heterostructure. *Phys. Rev. B* **100**, 014412 (2019).
- Chen, X. Z. et al. Control of spin current and antiferromagnetic moments via topological surface state. *Nat. Electron.* **5**, 574–578 (2022).
- Miron, I. M. et al. Perpendicular switching of a single ferromagnetic layer induced by in-plane current injection. *Nature* **476**, 189–193 (2011).
- Miron, I. M. et al. Current-driven spin torque induced by the Rashba effect in a ferromagnetic metal layer. *Nat. Mater.* **9**, 230–234 (2010).
- He, Q. L. et al. Tailoring exchange couplings in magnetic topological-insulator/antiferromagnet heterostructures. *Nat. Mater.* **16**, 94–100 (2017).
- Manna, P. K. & Yusuf, S. M. Two interface effects: exchange bias and magnetic proximity. *Phys. Rep.* **535**, 61–99 (2014).

15. Dong, R. R. et al. Exchange interactions in topological/antiferromagnetic heterostructures. *Appl. Phys. Lett.* **118**, 062410 (2021).
16. Yang, C. Y. et al. Termination switching of antiferromagnetic proximity effect in topological insulator. *Sci. Adv.* **6**, 8463 (2020).
17. He, Q. L. et al. Topological transitions induced by antiferromagnetism in a thin-film topological insulator. *Phys. Rev. Lett.* **121**, 096802 (2018).
18. He, Q. L. et al. Exchange-biasing topological charges by antiferromagnetism. *Nat. Commun.* **9**, 2767 (2018).
19. Pan, L. et al. Observation of quantum anomalous Hall effect and exchange interactions in topological insulator/antiferromagnet heterostructure. *Adv. Mater.* **32**, 2001460 (2020).
20. Xu, X. Y., Semenov, Y. G. & Kim, K. W. Spin wave generation via localized spin-orbit torque in an antiferromagnet-topological insulator heterostructure. *J. Appl. Phys.* **128**, 043901 (2020).
21. Zhao, W. J. et al. Magnetic proximity and nonreciprocal current switching in a monolayer WTe<sub>2</sub> helical edge. *Nat. Mater.* **19**, 503–507 (2020).
22. Higo, T. et al. Perpendicular full switching of chiral antiferromagnetic order by current. *Nature* **607**, 474–479 (2022).
23. Chen, X. Z. et al. Electric field control of Néel spin-orbit torque in an antiferromagnet. *Nat. Mater.* **18**, 931–935 (2019).
24. Chen, X. H. et al. Generation and control of terahertz spin currents in topology-induced 2D ferromagnetic Fe<sub>3</sub>GeTe<sub>2</sub>/Bi<sub>2</sub>Te<sub>3</sub> heterostructures. *Adv. Mater.* **34**, 2106172 (2022).
25. Qiu, H. S. et al. Ultrafast spin current generated from an antiferromagnet. *Nat. Phys.* **17**, 388–394 (2021).
26. Wu, X. J. et al. Antiferromagnetic-ferromagnetic heterostructure-based field-free terahertz emitters. *Adv. Mater.* **34**, 2204373 (2021).
27. Cong, K. K. et al. Coherent control of asymmetric spintronic terahertz emission from two-dimensional hybrid metal halides. *Nat. Commun.* **12**, 5744 (2021).
28. Agarwal, P., Huang, L. S., Lim, S. T. & Singh, R. Electric-field control of nonlinear THz spintronics emitters. *Nat. Commun.* **13**, 4072 (2022).
29. Khold, F. N. et al. The importance of the interface for picosecond spin pumping in antiferromagnet-heavy metal heterostructures. *Nat. Commun.* **14**, 538 (2023).
30. Seifert, T. et al. Efficient metallic spintronic emitters of ultrabroadband terahertz radiation. *Nat. Photon.* **10**, 483–488 (2016).
31. Huisman, T. J. et al. Femtosecond control of electric currents in metallic ferromagnetic heterostructures. *Nat. Nanotechnol.* **11**, 455–458 (2015).
32. Huang, L. et al. Antiferromagnetic magnonic charge current generation via ultrafast optical excitation. *Nat. Commun.* **15**, 4270 (2024).
33. Behovits, Y. et al. Terahertz Néel spin-orbit torques drive nonlinear magnon dynamics in antiferromagnetic Mn<sub>2</sub>Au. *Nat. Commun.* **14**, 6038 (2023).
34. Zhou, W., Wu, S. & Li, S. Relative stability, electronic structure, and magnetism of MnSe in rocksalt and zinc-blende structures. *J. Magn. Mater.* **395**, 166–172 (2015).
35. Jungfleisch, M. B. et al. Control of terahertz emission by ultrafast spin-charge current conversion at Rashba interfaces. *Phys. Rev. Lett.* **120**, 207207 (2018).
36. Zhou, C. et al. Broadband terahertz generation via the interface inverse Rashba-Edelstein effect. *Phys. Rev. Lett.* **121**, 086801 (2018).
37. Wang, X. et al. Ultrafast spin-to-charge conversion at the surface of topological insulator thin films. *Adv. Mater.* **30**, 1802356 (2018).
38. Gao, Y. et al. Chiral terahertz wave emission from the Weyl semimetal TaAs. *Nat. Commun.* **11**, 720 (2020).
39. Ali, S., Davies, J. R. & Mendonca, J. T. Inverse Faraday effect with linearly polarized laser pulses. *Phys. Rev. Lett.* **105**, 035001 (2010).
40. Higuchi, T., Kanda, N., Tamaru, H. & Gonokami, M. K. Selection rules for light-induced magnetization of a crystal with threefold symmetry: the case of antiferromagnetic NiO. *Phys. Rev. Lett.* **106**, 047401 (2011).
41. Satoh, T. et al. Spin oscillations in antiferromagnetic NiO triggered by circularly polarized light. *Phys. Rev. Lett.* **105**, 077402 (2010).
42. Ni, Z. L. et al. Giant topological longitudinal circular photo-galvanic effect in the chiral multifold semimetal CoSi. *Nat. Commun.* **12**, 154 (2021).
43. Liu, Y. X. et al. Magnetic proximity effect in an antiferromagnetic insulator/topological insulator heterostructure with sharp interface. *Chin. Phys. Lett.* **38**, 057303 (2021).
44. Wang, R., Ding, J. W., Sun, F., Zhao, J. M. & Qiu, X. H. Photodoping-modified charge density wave phase transition in WS<sub>2</sub>/1T-TaS<sub>2</sub> heterostructure. *Chin. Phys. Lett.* **41**, 057801 (2024).
45. Yuto, K. et al. Terahertz radiation by subpicosecond magnetization modulation in the ferrimagnet LiFe<sub>5</sub>O<sub>8</sub>. *ACS Photo* **3**, 1170–1175 (2016).

## Acknowledgements

This work was financially supported by the National Key Research and Development Program of China (Grant Nos. 2024YFA1408700, 2021YFA1400201, 2022YFA1403800, and 2022YFA1604402), CAS Project for Young Scientists in Basic Research (Grant No. YSBR-059), CAS Interdisciplinary Innovation Team, International Partnership Program of Chinese Academy of Sciences (Grant No. GJHZ1826), National Natural Science Foundation of China (Grant Nos. 11774408, 92250307 and 12274445), Beijing Natural Science Foundation (Grant No. 4191003), and the Youth Innovation Promotion Association of the Chinese Academy of Sciences.

## Author contributions

J.Z. conceived the idea and lead the project. Y.C. and P.G. conducted the ultrafast THz spectroscopy experiment. J.T. and Y.L. fabricated the sample and performed the characterization. Y. C., J.T., P.L. and J.Z. analyzed the data. Y.C., X.W., F.K. and J.Z. discussed the mechanism. Y.C., F.Z. L.J., and J.Z. wrote the paper with input from all authors.

## Competing interests

The authors declare no competing interests.

## Additional information

**Supplementary information** The online version contains supplementary material available at <https://doi.org/10.1038/s41467-025-60060-5>.

**Correspondence** and requests for materials should be addressed to Jing Teng or Jimin Zhao.

**Peer review information** *Nature Communications* thanks the anonymous, reviewers for their contribution to the peer review of this work. A peer review file is available.

**Reprints and permissions information** is available at <http://www.nature.com/reprints>

**Publisher's note** Springer Nature remains neutral with regard to jurisdictional claims in published maps and institutional affiliations.

**Open Access** This article is licensed under a Creative Commons Attribution-NonCommercial-NoDerivatives 4.0 International License, which permits any non-commercial use, sharing, distribution and reproduction in any medium or format, as long as you give appropriate credit to the original author(s) and the source, provide a link to the Creative Commons licence, and indicate if you modified the licensed material. You do not have permission under this licence to share adapted material derived from this article or parts of it. The images or other third party material in this article are included in the article's Creative Commons licence, unless indicated otherwise in a credit line to the material. If material is not included in the article's Creative Commons licence and your intended use is not permitted by statutory regulation or exceeds the permitted use, you will need to obtain permission directly from the copyright holder. To view a copy of this licence, visit <http://creativecommons.org/licenses/by-nc-nd/4.0/>.

© The Author(s) 2025